

Article

Flexible Films as Anode Materials Based on rGO and TiO₂/MnO₂ in Li-Ion Batteries Free of Non-Active Agents

Tomasz Kędzierski ^{1,*} , Daria Baranowska ¹ , Damian Bęben ^{2,3}, Beata Zielińska ^{1,*}, Xuecheng Chen ¹ and Ewa Mijowska ¹

¹ Department of Nanomaterials Physicochemistry, Faculty of Chemical Technology and Engineering, West Pomeranian University of Technology in Szczecin, Piastów 45, 70-311 Szczecin, Poland; bd36293@zut.edu.pl (D.B.); xuecheng.chen@zut.edu.pl (X.C.); ewa.borowiak-palen@zut.edu.pl (E.M.)

² Nanores Sp. z o.o. Sp.k., Bierutowska 57-59, 51-317 Wrocław, Poland; damian.beben@nanores.pl

³ Institute of Low Temperature and Structure Research, Polish Academy of Sciences in Wrocław, Okólna 2, 50-420 Wrocław, Poland

* Correspondence: tomasz.kedzierski@zut.edu.pl (T.K.); beata.zielinska@zut.edu.pl (B.Z.)

Abstract: Recently, to meet the growing demand for stable and flexible batteries, anodes in the form of thin films have drawn the attention of researchers. It is clear that mass production of such batteries would bring the worldwide distribution of flexible devices and wearable electronics closer. Currently, electrodes are deposited on a flexible substrate and consist of conductive and binding agents that increase the volume/weight of the electrode. Here, we propose free-standing and non-active-material-free thin films based on reduced graphene oxide (rGO), titanium dioxide (TiO₂) and manganese dioxide (MnO₂) as working electrodes in lithium-ion half-cells prepared via the vacuum-assisted filtration method. The electrochemical performance of the assembled half-cells exhibited good cyclic stability and a reversible capacity at lower current densities. The addition of TiO₂ and MnO₂ improved the capacity of the rGO film, while rGO itself provided a stable rate performance. rGO/TiO₂/MnO₂ film showed the highest discharge capacity (483 mAh/g at 50 mA/g). In addition, all assembled cells displayed excellent repeatability and reversibility in cyclic voltammetry measurements and good lithium-ion diffusion through the electrolyte, SEI layer and the active material itself.

Keywords: Li-ion batteries; thin-film growth; reduced graphene oxide; vacuum-assisted filtration



Citation: Kędzierski, T.; Baranowska, D.; Bęben, D.; Zielińska, B.; Chen, X.; Mijowska, E. Flexible Films as Anode Materials Based on rGO and TiO₂/MnO₂ in Li-Ion Batteries Free of Non-Active Agents. *Energies* **2021**, *14*, 8168. <https://doi.org/10.3390/en14238168>

Academic Editors: Alon Kuperman and Alessandro Lampasi

Received: 15 November 2021

Accepted: 2 December 2021

Published: 6 December 2021

Publisher's Note: MDPI stays neutral with regard to jurisdictional claims in published maps and institutional affiliations.



Copyright: © 2021 by the authors. Licensee MDPI, Basel, Switzerland. This article is an open access article distributed under the terms and conditions of the Creative Commons Attribution (CC BY) license (<https://creativecommons.org/licenses/by/4.0/>).

1. Introduction

Due to the constant utilization of fossil fuels and their negative impact on the environment, researchers around the world are persistently searching for energy storage systems that would not emit greenhouse gases nor pollute the environment [1]. In addition, there is an ongoing demand for high-tech and multifunctional portable products, for example, wearable electronics, bendable smartphones and displays. Because of this, energy storage systems in these devices should have matching mechanical properties, allowing them to tolerate deformation while maintaining their electrochemical functions [2].

Lithium-ion batteries (LIBs) are the most prominent power sources for electronic devices because of their high energy density, power density, mechanical stability and rate capability [3]. The cathode materials are usually made of LiCoO₂ or LiMn₂O₄. The cathode, being the source of lithium, determines the average voltage of the battery and its capacity. The cobalt-based electrodes are great for their high volumetric capacity, low self-discharge, high discharge voltage and good cycling performance, but they are quite expensive and have low thermal stability. The manganese-based cathodes are suitable due to their low cost, but nevertheless, they also have some limitations, including the tendency of manganese to dissolve into the electrolyte, leading to poor cycling stability

of the positive electrode [4]. The role of the anode is to store (during charging) and release (during discharging) lithium ions originating from the cathode. Currently, the most commercially used anode material is graphite, with a maximum theoretical capacity of 372 mAh/g [5]. Hence, many researchers developed new anode materials with higher capacities, such as transition-metal oxides [6,7] or other carbon-based materials, such as graphene, carbon nanotubes [8,9] and their composites [10,11]. Graphene and its derivatives have many distinctive properties, such as a large specific surface area ($2630 \text{ m}^2/\text{g}$) [12], a high thermal conductivity ($3000\text{--}5000 \text{ W/mK}$) [13] and a high carrier mobility at room temperature ($\sim 10,000 \text{ cm}^2/\text{Vs}$) [14]. The graphene derivatives graphene oxide (GO) and reduced graphene oxide (rGO), which are terminated with oxygen groups that allow for the tuning of the properties of these materials, are known for their low-cost and mass production [15,16]. Due to their remarkable properties, graphene-based composites are excellent candidates for anode materials for lithium-ion batteries and a lot of research is being conducted to improve their electrochemical performance. As an alternative to full cells, the electrochemical nature of Li-ion batteries can be examined in a half-cell configuration, where metallic lithium acts as both the reference and the counter electrode (the cathode), while a carbon material acts as the working electrode (the anode). Due to a stable reference potential, as well as a very large reservoir of capacity, the reactions at the working electrode are limited by the capacity of the counter electrode [17]. For instance, Joshi et al. [18] fabricated a half-cell where an electrosprayed composite made of graphene sheets decorated with pillar-like ZnFe_2O_4 nanoparticles acted as the working electrode/the anode. This anode material showed a high capacity, good rate capability and long-term cycling stability in comparison to cells free of graphene. The specific capacity at the current density of 100 mA/g was approximately 1100 mAh/g and stayed at that level after 30 cycles. Dong et al. [19] prepared a graphene- WS_2 multilayer film via water-evaporation-induced assembly and chemical reduction. Due to improved contact between the graphene and WS_2 , the material exhibited a high specific capacity, an effective cycling performance and a high rate capability. Moreover, the fast lithium-ion migration was attributed to the microcavities inside the material. Fang et al. [20] synthesized CoO/rGO film on Ti foil via the electrodeposition method. The composite showed an initial capacity of 1290 mAh/g under a current density of 100 mA/g and 766 mAh/g under 1000 mA/g.

Regarding other rGO/ TiO_2 electrodes, Dong et al. [21] hydrothermally synthesized an rGO composite with TiO_2 nanorods. This material displayed a high rate capacity (up to 10 C) and a specific capacity of 347 mAh/g at 0.2 C that remained stable after 20 cycles. Tang et al. [22] prepared a TiO_2 /graphene nanocomposite by mixing and sonicating both materials. Their composite showed an initial specific capacity of 389 mAh/g at 100 mA/g of current density; however, it was not stable and the capacity gradually decreased. For an rGO/ MnO_2 composite, Xu et al. [23] obtained MnO_2 /graphene films via electrophoretic deposition (EPD). Their material delivered a high specific capacity, even after 200 cycles. Despite such extended research, new materials for anodes are being developed every day to further increase the performance of flexible lithium-ion batteries without non-active components such as binding or conductive agents.

In this study, flexible, non-active-material-free thin films based on reduced graphene oxide (rGO), titanium dioxide (TiO_2) and manganese dioxide (MnO_2) have been fabricated by the vacuum-assisted filtration method (VAF). The obtained films (rGO, rGO/ TiO_2 , rGO/ MnO_2 and rGO/ TiO_2 / MnO_2) were binder-free (such as polyvinylidene fluoride (PVDF)) and without a conductive agent (such as carbon black). These anode materials for lithium-ion half-cells, and their performances, have been tested in great detail. More interestingly, an additional current collector such as Al or Cu foil was redundant in the configuration of the lithium-ion half-cells, which made the electrode much lighter than a typical tablet or as a slurry deposited on a collector. What is more, no toxic solvent, such as NMP, was used during electrode preparation. Therefore, in this approach, a low-cost and environmentally friendly process for the production of thin, free standing and flexible films serving as anodes in Li-ion half-cells has been designed. Additionally, these films displayed

flexibility, bendability, and excellent repeatability, reversibility and rate performance as working electrodes in lithium-ion batteries.

2. Materials and Methods

2.1. Materials

Titanium dioxide (TiO_2 , A450; particle size 3–7 nm) was purchased from Grupa Azoty (Police, Poland). Potassium permanganate (KMnO_4), oxalic acid dihydrate ($\text{C}_2\text{H}_6\text{O}_6 \cdot \text{H}_2\text{O}$), sulfuric acid (H_2SO_4 , 95%) and orthophosphoric acid (H_3PO_4 , 85%) were acquired from Chempur (Piekary Śląskie, Poland). Hydrogen peroxide (H_2O_2 , 30%) was bought from PPUH “Tarchem” Sp. z o.o. (Tarnowskie Góry, Poland). 1 M lithium hexafluorophosphate solution (LiPF_6) and lithium foil were purchased from Sigma-Aldrich (Poznań, Poland). Graphite flakes (~325 mesh, 99.8%) and hydrochloric acid (HCl , 35–37%), were purchased from Alfa Aesar (Kandel, Germany) and P. P. H. “STANLAB” Sp. z o.o. (Lublin, Poland), respectively. The membrane used in the film formation process was Whatman Cyclopure Polycarbonate Track Etched Membrane (diameter 0.4 μm).

2.2. Synthesis of Graphene Oxide (GO)

A modified Hummers’ method was used to prepare graphene oxide. Briefly, 135 mL of a mixture of concentrated H_2SO_4 and H_3PO_4 (ratio = 8:1) was poured onto 1 g of graphite and 6 g of KMnO_4 and stirred for 24 h at 50 °C. After the reaction, the mixture was poured into a cold solution of hydrogen peroxide (1 mL per 150 mL of H_2O), then centrifuged and washed alternately with water, hydrochloric acid (30%) and ethanol. Finally, the GO was dried in air at 60 °C for 12 h.

2.3. Synthesis of Manganese Dioxide (MnO_2)

Manganese dioxide was synthesized by a method reported by Cao et al. [24]. Shortly, 1.58 g of KMnO_4 was dissolved in 60 mL of distilled water (DW) and, separately, 2.28 g of oxalic acid was dissolved in 100 mL of water. After both materials were dissolved, the KMnO_4 solution was slowly added to the oxalic acid solution. Next, the mixture was stirred for 2 h and then filtrated. The obtained precipitate was washed with water and dried at 90 °C for 12 h.

2.4. Thin Film Preparation

Thin films were prepared via the vacuum-assisted filtration (VAF) method. The composition of the obtained films (rGO, rGO/ TiO_2 , rGO/ MnO_2 and rGO/ TiO_2 / MnO_2) is shown in Table 1, as well as the thickness, measured via scanning electron microscopy. Briefly, the following dispersions were prepared: 5 mg of GO in 100 mL of DW, 1 mg of TiO_2 in 100 mL of DW and 1 mg of MnO_2 in 100 mL of DW. Each mixture was sonicated until a homogeneous dispersion was achieved. After that, 5 mL of the appropriate dispersion was introduced to the microfiltration set to form the desired films. The procedure was repeated about 70 times until films of the desired thickness were fabricated (see Table 1). The obtained films were dried at room temperature, peeled off of the PC membrane and thermally reduced at 400 °C for 2 h in inert gas conditions. The reduction of GO to rGO was performed to improve the film’s conductivity and electrochemical responses. The structures of the produced films are presented in Figure 1.

Table 1. Composition of each film, produced via VAF method.

Film	WEIGHT RATIO			Thickness [μm]
	GO	TiO_2	MnO_2	
rGO	5	0	0	10.86
rGO/ TiO_2	5	1	0	2.66
rGO/ MnO_2	5	0	1	2.79
rGO/ TiO_2 / MnO_2	5	1	1	2.29

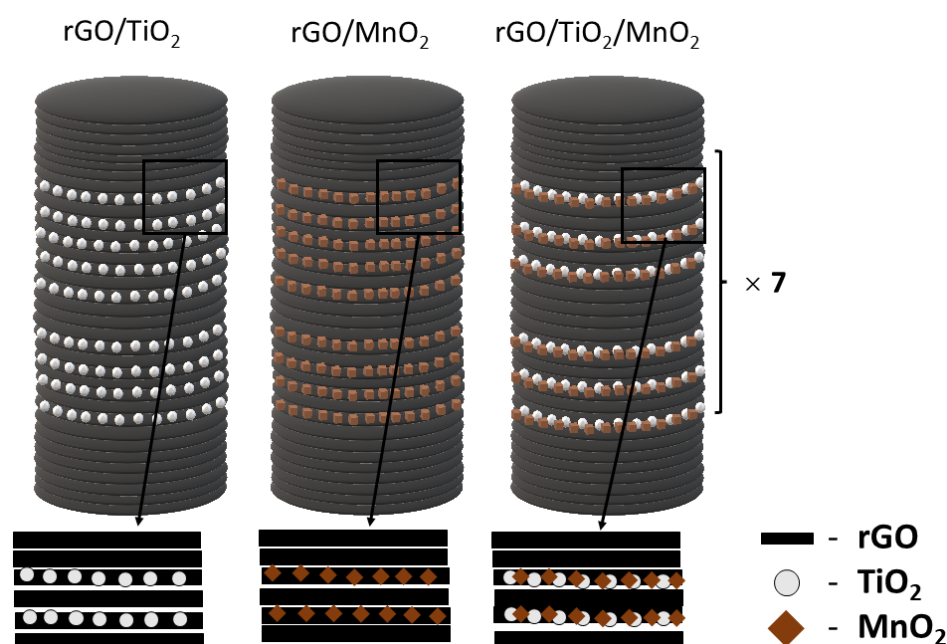


Figure 1. Schematic drawing of the rGO-based films prepared via the VAF method.

2.5. Electrochemical Measurement

The coin cells (CR2032) were assembled inside the Ar-filled glovebox (M. Braun Inertgas-Systeme GmbH, Garching, Germany). Constructed cells were built in a half-cell configuration, where a 15 mm disc of metallic lithium was used as both the reference and counter electrodes and a 12 mm disc of each film acted as working electrodes. Reference TiO_2 and MnO_2 electrodes were prepared in the form of tablets with the addition of carbon black and PVDF in the ratios of 8:1:1 for TiO_2 and 4.5:4.5:1 for MnO_2 . The increased amount of carbon black in the MnO_2 -based electrodes was used due to the material pulverizing after discharge/charge cycles. This procedure allowed the electrode to be buffered more effectively. The electrolyte (1 M LiPF_6 solution in ethylene carbonate and diethyl carbonate) was used to wet both glass fiber and Celgard[®] separators (polypropylene/polyethylene). Before the actual electrochemical test, the cells were connected to the channels for 8 h during the OCV technique. All electrochemical measurements were performed using a BioLogic VMP3 instrument (BioLogic, Seyssinet-Pariset, France) at room temperature. The cells were charged and discharged over a voltage range of 0 to 3 V vs. Li/Li^+ at room temperature. Cyclic voltammetry (CV) was performed in the same range at a scan rate of 0.1 mV/s. Electrochemical impedance spectroscopy (EIS) was executed in the frequency range from 100 to 10 mHz. Open circuit voltage (OCV) was turned on between techniques to stabilize the potential. Galvanostatic cycling with potential limitation (GCPL) was used to examine the specific capacity of the assembled cells during 5 cycles at the current densities: 50, 100, 200, 400, 600, 1000, 2000, 5000, 10,000 and back at 50 mA/g.

2.6. Material Characterization

Scanning electron microscopy (SEM) was performed using the SEM column of SEM/Ga-FIB FEI Helios NanoLab[™] 600i dualbeam microscope (FEI Company, Hillsboro, OR, USA). Transmission electron microscopy (TEM, Tecnai F30 with a field emission gun operating at 200 kV, Thermo Fisher Scientific, Waltham, MA, USA) with an energy dispersive X-ray spectrometer (EDX) was used to view both the morphology and the elemental distribution of the prepared films. A Renishaw InVia Raman microscope (Renishaw, New Mills Wotton-under-Edge, UK) ($\lambda = 785$ nm) was used for vibronic characterization of the samples. The phase composition analysis of the films was performed using an Aeris diffractometer (Malvern Panalytical, Malvern, UK) and $\text{Cu-K}\alpha$ radiation ($\lambda = 1.544$ Å).

3. Results and Discussion

3.1. Transmission Electron Microscopy

A TEM analysis, shown in Figure 2a–d, was used to reveal the morphology of the prepared films. Here, the samples were prepared by dropping GO, TiO₂ and/or MnO₂ dispersions directly on the TEM grid. Additionally, Figure 2 shows digital images of the prepared films (Figure 2e–h) and their flexible behaviors are shown with a caliper set on 100 mm (Figure 2i–l). TEM images of pristine TiO₂ and MnO₂ are presented in Figure S1. GO exhibited typical wrinkled and folded morphology (Figure 2a). The GO flakes had a wide range of sizes, ranging from few dozen to a few hundred nanometers. Titanium dioxide particles deposited on GO flakes (Figure 2b), demonstrated a tendency to agglomerate into a large irregular form. Manganese dioxide particles (Figure 2c) showed a similar morphology. Figure 2d depicts GO/TiO₂/MnO₂ with clear TiO₂ and MnO₂ agglomerates. To study the elemental composition of the produced films energy-dispersive X-ray spectroscopy (EDX) measurements were performed (Figure 3). The results displayed that carbon, oxygen and titanium; carbon, oxygen and manganese; and carbon, oxygen, titanium and manganese are the only elements in GO/TiO₂, GO/MnO₂ and GO/TiO₂/MnO₂, respectively. Carbon was detected from both GO flakes and the TEM grid.

3.2. Scanning Electron Microscopy

Figure 4 shows cross-sectional and topography images of the rGO, rGO/TiO₂, rGO/MnO₂ and rGO/TiO₂/MnO₂ films. The rGO film (Figure 4a) displayed a loosely stacked structure with large, empty spaces between rGO layers. rGO/TiO₂ (Figure 4b) exhibited large agglomerates of TiO₂ located between rGO layers. rGO/MnO₂ (Figure 4c) presented small particles of MnO₂ placed inside the pores of rGO. In rGO/TiO₂/MnO₂ film (Figure 4d) large agglomerates of TiO₂ and particles of MnO₂ could be seen inside rGO pores. The nanoadditives held together the rGO structure, while pristine rGO tended to expand inward, creating vast and empty spaces, explaining the approximately three times larger thickness of pristine rGO compared to that of the composites. Moreover, Figure 4e–h shows topography images of rGO, rGO/TiO₂, rGO/MnO₂ and rGO/TiO₂/MnO₂, respectively. The tops of all films were covered with extra rGO layers displaying folded and irregular forms.

3.3. X-ray Diffraction

XRD patterns of the obtained films are presented in Figure 5 (patterns were collected directly from the surface of the films). Additionally, the patterns of the reference TiO₂ and MnO₂ electrodes are shown in Figure S2. TiO₂ is composed of two crystalline phases: anatase and rutile. Here, the diffraction reflections at ~25.3, 37.7, 47.8, 53.9, 54.8, 62.5, 68.7, 70.1, 74.9 and 82.6° that matched the 102, 004, 200, 105, 211, 204, 116, 220, 215 and 312 indexes were related to the anatase phase (ICSD card no. 009853) and the reflections at ~27.4–110, 36.1–101, and 41.2°–111, associated with rutile phase (ICSD card no. 165920), were observed. MnO₂ exhibited several reflections located at ~12.9, 18.2, 25.9, 28.8, 37.7, 42.1, 49.9, 56.3, 60.2, 65.6, 69.2 and 73.1° corresponding to the 110, 200, 220, 130, 211, 301, 141, 600, 251, 002, 541 and 132 indexes of tetragonal α -MnO₂ (ICSD card no. 073363), respectively. rGO displayed one clear reflection at ~25°, which came from the 002 diffraction plane. The presence of this reflection and the absence of a reflection at ~11° confirmed that GO was reduced successfully [25]. The characteristic reflection attributed to rGO was identified in the rGO/TiO₂, rGO/MnO₂ and rGO/TiO₂/MnO₂ patterns. Moreover, those films showed low-intensity reflections of TiO₂ (rGO/TiO₂), MnO₂ (rGO/MnO₂) and both TiO₂ and MnO₂ (rGO/TiO₂/MnO₂).

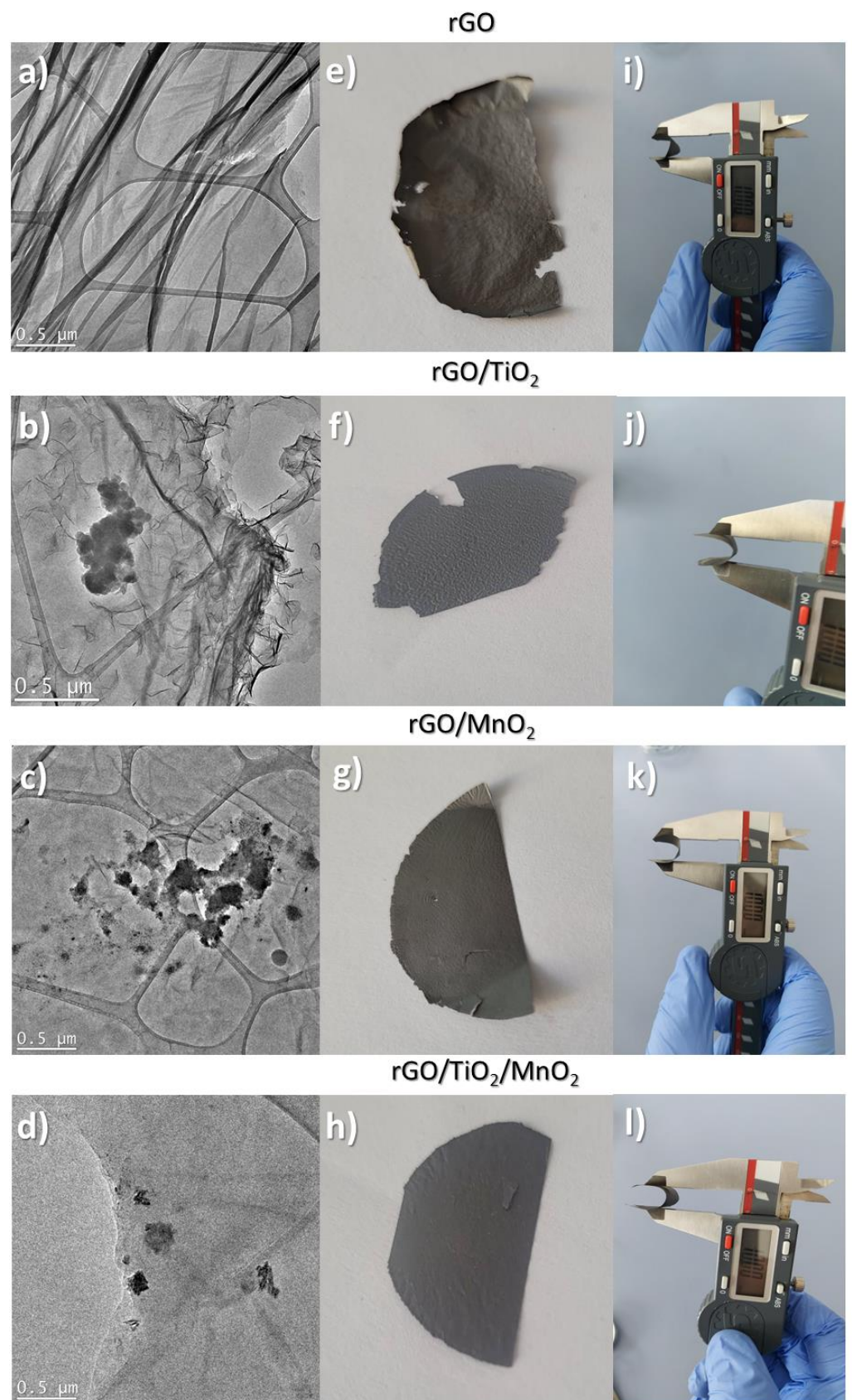


Figure 2. TEM images (a–d), photographs (e–h) and flexibility measured with a caliper (i–l) of the rGO, rGO/TiO₂, rGO/MnO₂ and rGO/TiO₂/MnO₂ films.

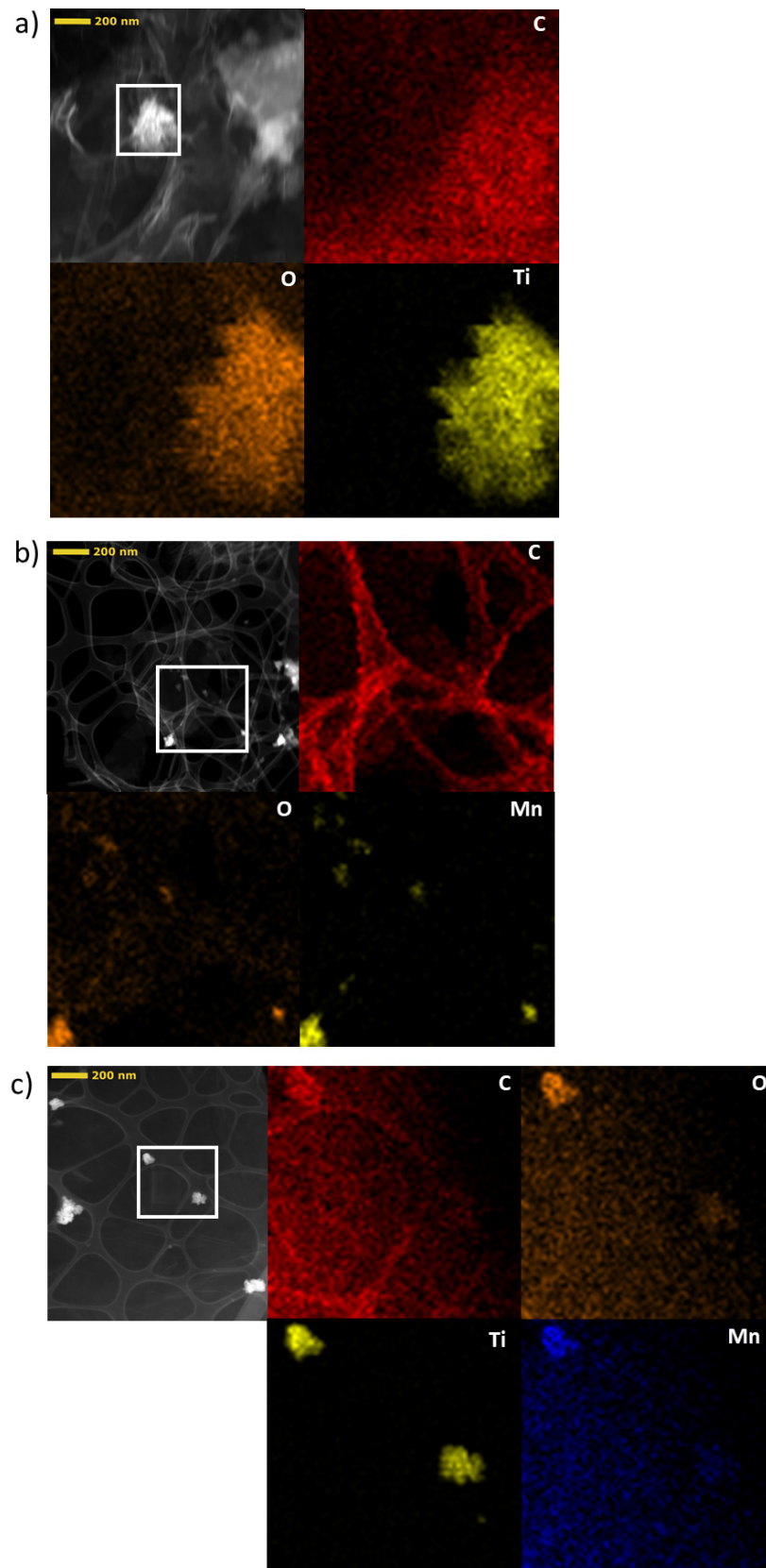


Figure 3. Drift-corrected spectrum image scanning and elemental mapping of the (a) GO/TiO₂, (b) GO/MnO₂ and (c) GO/TiO₂/MnO₂ films.

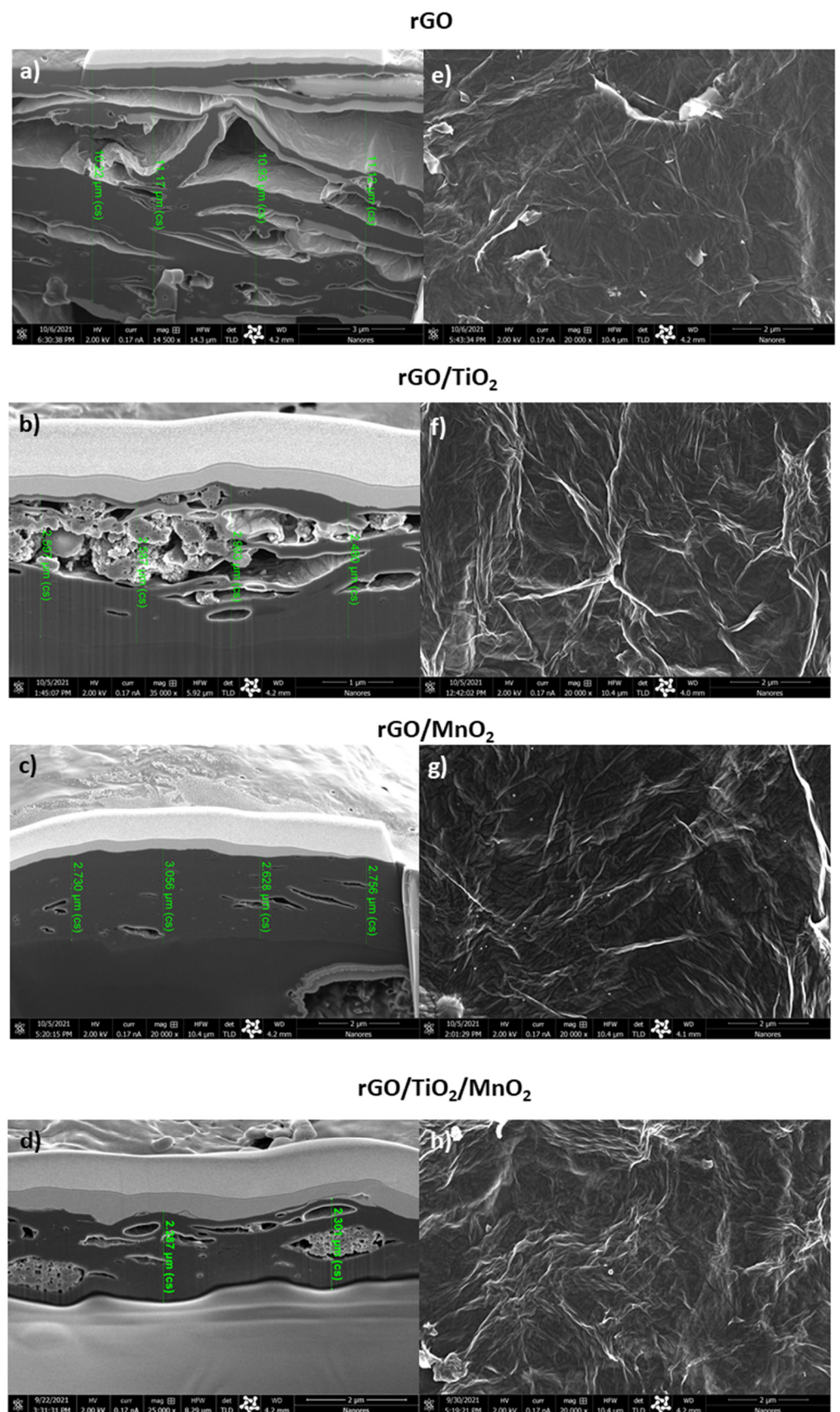


Figure 4. SEM images presenting cross section (a–d) and topography (e–h) of the rGO, rGO/TiO₂, rGO/MnO₂ and rGO/TiO₂/MnO₂ films.

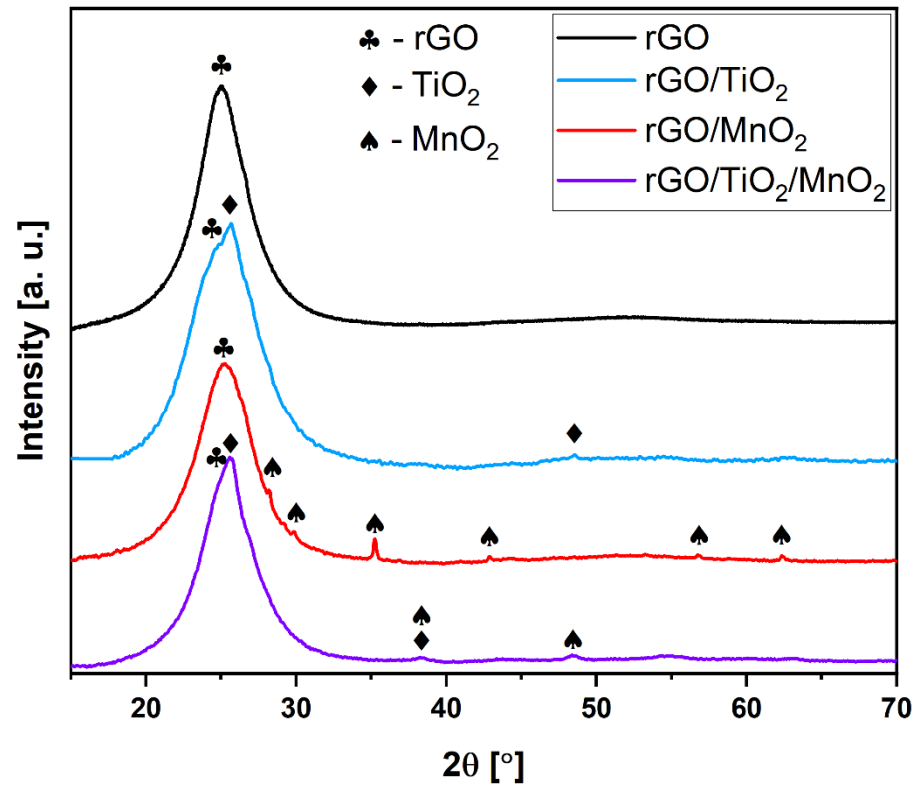


Figure 5. XRD patterns of the rGO-based films.

3.4. Raman Spectroscopy

Figure 6 displays the Raman spectra of the rGO-based films. Every spectrum had the typical bands for carbon materials: D at 1324 cm^{-1} and G at 1604 cm^{-1} . The first band was caused by basal plane defects in the carbon structure. The second band was related to in-plane stretching vibration of the C-C structure, in sp^2 systems [26]. The band at 151 cm^{-1} in the rGO/TiO₂ spectrum was assigned to the E_g vibrational mode of TiO₂ [27]. rGO/MnO₂ showed a characteristic band at 646 cm^{-1} that corresponded to Mn-O stretching vibration [28]. The rGO/TiO₂/MnO₂ spectrum showed characteristic bands for rGO, TiO₂ and MnO₂, with slight shifts due to the additional components. Furthermore, the peak at 429 cm^{-1} could be attributed to a mixture of titanium and manganese oxides [29]. Additionally, the Raman modes of reference for TiO₂ and MnO₂ are presented in the Supplementary information (Figure S3). MnO₂ showed strong peaks at $\sim 181, 283, 306, 370, 513, 582, 635$ and 654 cm^{-1} , which confirmed the α -MnO₂ structure [30]. TiO₂ displayed peaks at $\sim 142, 395, 516$ and 638 cm^{-1} , corresponding to the E_g, B_{1g}, A_{1g} and E_g modes of the anatase phase, respectively [27].

3.5. Electrochemical Measurements

To validate the electrochemical potential of the assembled films, lithium-ion batteries were constructed in a half-cell configuration. Metallic lithium acted as both the reference and counter electrodes, while rGO-based films acted as the working electrode. The cyclic performances of the rGO-based films are shown in Figure 7. Figure 7a presents the cyclic voltammograms (CV) of the rGO film, which did not exhibit any redox peaks. The black curve displaying the first cycle of charge/discharge diverges from the next cycles due to the irreversible formation of the SEI layer. The subsequent curves are overlapping each other, which means that delithiation/lithiation process was repeatable. In Figure 7b (rGO/TiO₂), two peaks can be observed at 2.04 and 1.75 V, which correspond to the

oxidation and reduction reactions, respectively. The electrochemical reduction/oxidation (lithiation/delithiation) of TiO_2 is described below [31]:

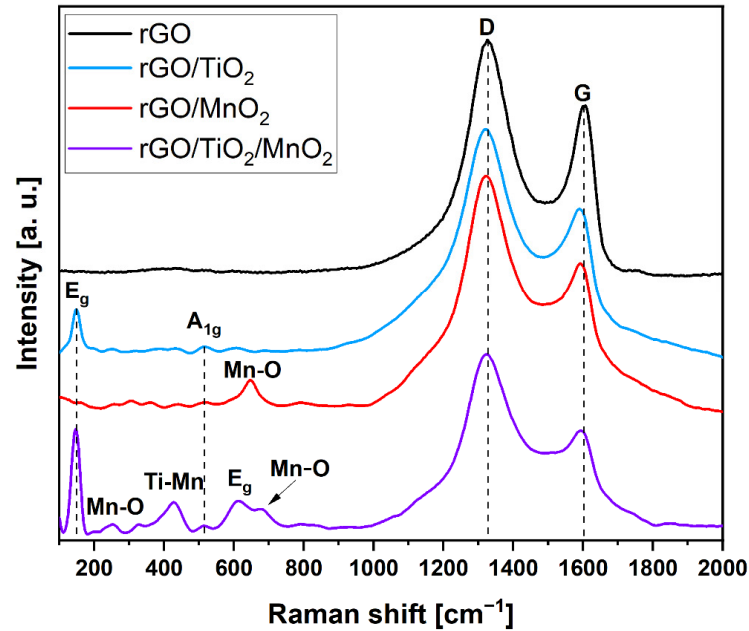
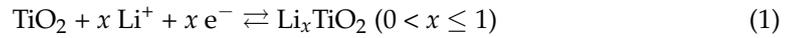


Figure 6. Raman spectra of the rGO-based films. The measurements were conducted with an excitation wavelength of 785 nm.

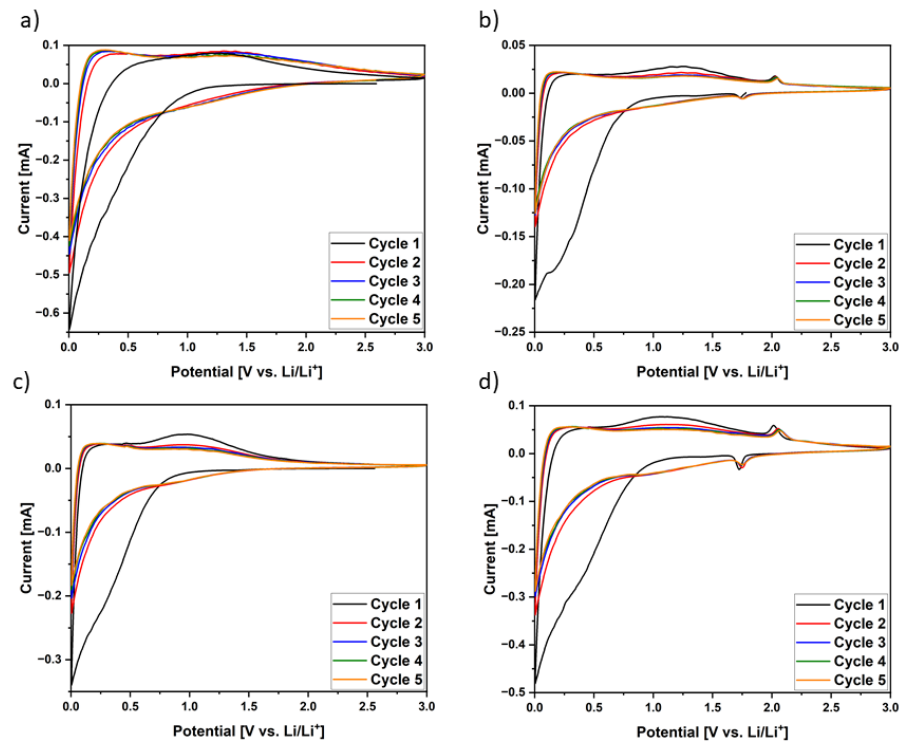


Figure 7. Cyclic voltammograms recorded over a potential window 0.005 to 3 V at a scan rate 0.1 mV/s for the (a) rGO, (b) rGO/TiO₂, (c) rGO/MnO₂ and (d) rGO/TiO₂/MnO₂ films.

Figure 7c shows the CV of the rGO/MnO₂ film, which did not exhibit any characteristic peaks of manganese dioxide. Moreover, Figure 7d (rGO/TiO₂/MnO₂) presents peaks coming only from TiO₂. Figure S4 shows CV plots of TiO₂ and MnO₂, respectively. The first cycle of the TiO₂ cyclic performance (Figure S4a) exhibited intense peaks of oxidation and reduction reactions at 2.18 and 1.57 V, respectively. Their intensity was reduced in the following cycles due to the poor cyclic stability of TiO₂. Moreover, the SEI formation in the range from 0.01 to 0.56 V could be seen. Figure S4b presents the cyclic performance of MnO₂. The first cycle displayed two peaks in the discharging/lithiation region: the first peak, at 0.1 V, corresponded to the reduction of Mn⁴⁺ to Mn⁰ [32], and the second peak, at 0.57 V, corresponded to the SEI layer formation. In the charging/delithiation region there was one peak, at 1.27 V, indicating the oxidation of Mn⁰ to Mn²⁺. The reduction/oxidation process of manganese dioxide is described by the equation below [32]:



Figure 8 displays the first, third and fifth cycles of the galvanostatic charge/discharge curves of each film at 50 mA/g, recorded between 0.005 and 3.0 V. The starting discharge/charge capacities were 411/388, 400/372, 402/387 and 482/470 mAh/g for rGO, rGO/TiO₂, rGO/MnO₂ and rGO/TiO₂/MnO₂, respectively. However, in the following cycles, rGO/MnO₂ discharge/charge capacity exceeded that of rGO. In the subsequent cycles each material exhibited a stable discharge/charge capacity, displaying the excellent reversibility and outstanding cycling stability of rGO-based films. The slight increase in the capacities of the films was caused by the agglomeration of TiO₂ and the small amount of MnO₂ that was also concealed by rGO. Figure S5 presents the discharge/charge profiles of pristine TiO₂ and MnO₂. The initial discharge/charge capacity of TiO₂ was 64/52 mAh/g and 972/896 mAh/g for MnO₂. The latter displayed better cyclic stability than TiO₂ and a much higher capacity. During charging, intercalating lithium expands any active material particles, which pulverizes the electrode. This phenomenon was extremely noticeable in MnO₂. Therefore, despite its great initial capacity, the MnO₂ electrode required a buffer to stabilize the active material and extend the electrochemical performance. For this reason, we proposed combining MnO₂ with GO in the form of a film, so that GO (later rGO) could shield MnO₂ against overexpansion.

It is crucial to examine the anode performance at lower-to-higher current densities to comprehend the current capacity of the active material. Hence, all films were submitted to electrochemical testing at different current densities from 50 to 10,000 mA/g (Figure 9). Each electrode exhibited a more stable cyclic performance at higher current densities. For instance, at 50 mA/g the specific discharge capacity of the rGO/TiO₂/MnO₂ film (Figure 9d) decreased from 482 to 433 mAh/g, while at 200 mA/g it decreased from 272 to 260 mAh/g. Moreover, when cycled back at a lower current density of 50 mA/g, the cell regained the specific capacity of a current density of 100 mA/g. Such satisfactory reversible performance may have been due to the great degree of graphitization of rGO. Moreover, it is worth noting that after the addition of TiO₂ nanoparticles (Figure 9b) the specific capacity of the rGO film increased at higher current densities, while the addition of MnO₂ particles (Figure 9c) elevated the specific capacity of the rGO film at lower current densities. Such a great capacity of the films was due to the highly graphitized rGO which allowed smooth lithium diffusion through the porous and slit-like morphology. Figure S6 shows the rate performance of pristine TiO₂ and MnO₂ at different current densities. TiO₂ displayed a poor specific capacity and an inferior rate performance when current densities over 50 mA/g were applied, decreasing to 0 mAh/g over 400 mA/g. However, when cycled back at 50 mA/g the capacity exceeded that of 100 mA/g, which was not the case for rGO-based films. The unusually poor performance of TiO₂ may have been attributed to the strong tendency of TiO₂ nanoparticles to agglomerate, which in turn limited the active surface where Li⁺ could be attached. Figure S6b exhibits the rate performance of MnO₂. This material manifested a high specific discharge/charge capacity at 50 mA/g ranging from 972/918 mAh/g to 887/868 mAh/g for the first and the fifth cycle, respectively.

Moreover, it presented an outstanding cyclic stability and its rate performance was slightly lower than that of the films. Furthermore, the cycles repeated at 50 mA/g displayed slightly lower specific capacities.

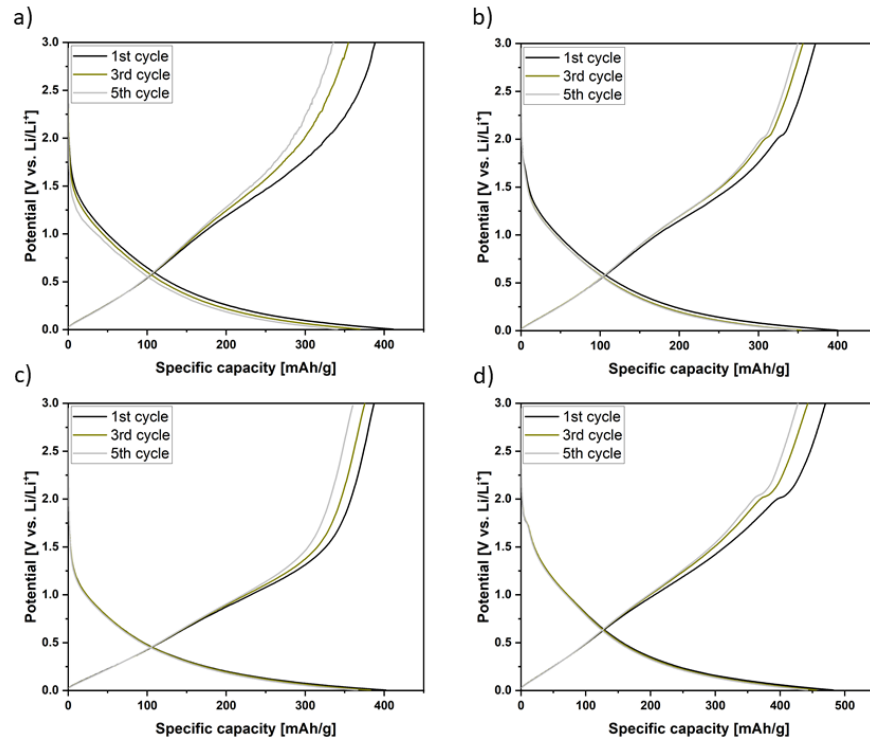


Figure 8. Discharge/charge profiles of the (a) rGO, (b) rGO/TiO₂, (c) rGO/MnO₂ and (d) rGO/TiO₂/MnO₂ films at a current density of 50 mA/g.

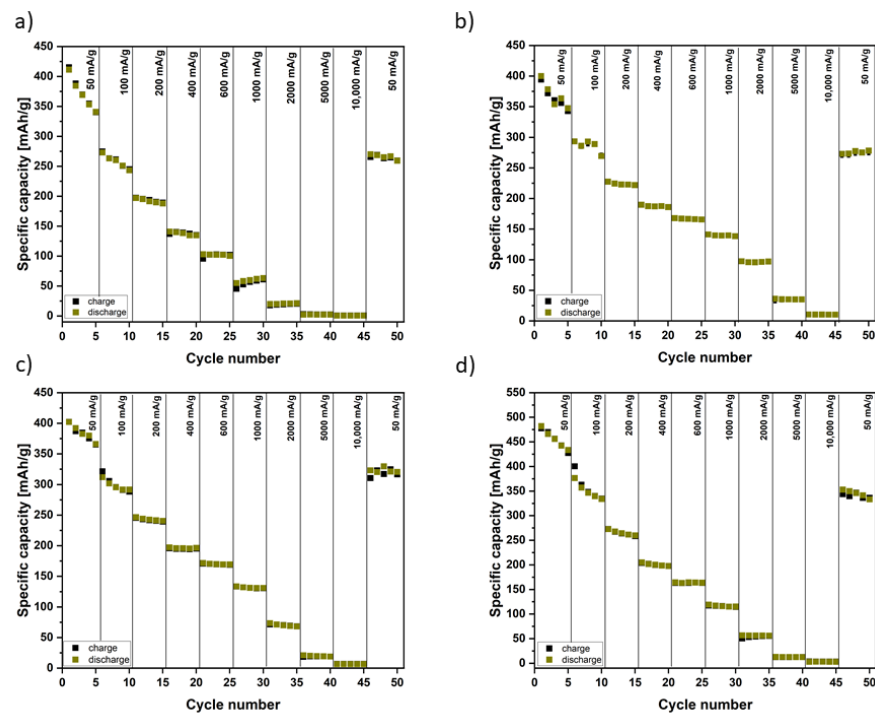


Figure 9. Rate performance of the (a) rGO, (b) rGO/TiO₂, (c) rGO/MnO₂ and (d) rGO/TiO₂/MnO₂ films at different current densities.

EIS measurements were conducted on the half-cells over a range of frequencies from 100 kHz to 10 mHz and the recorded Nyquist plots are shown in Figure 10. This technique helped to further interpret Li-ion storage exploitation. The rGO (Figure 10a), rGO/TiO₂ (Figure 10b) and rGO/MnO₂ (Figure 10c) plots display a single semicircle and a steep diagonal line (Warburg line). However, the rGO/TiO₂/MnO₂ (Figure 10d) plot exhibits an additional, weaker semicircle and a gentler slope. The equivalent circuit diagrams used to calculate the EIS results and the fitting parameters are presented in Table 2. R_s (solution resistance), R_{SEI} (SEI layer resistance) and R_{ct} (charge-transfer resistance) were established by the fitted lines shown in Figure 10. The R_{SEI} was not present in the rGO, rGO/TiO₂ and rGO/MnO₂ samples, which indicated the smoother lithium-ion migration through the SEI layer. In comparison, for rGO/TiO₂/MnO₂ the R_{SEI} value (181.1 Ω) implied a slightly more resilient Li⁺ migration through the SEI interface. Remarkably, the R_{ct} (charge-transfer resistance) of rGO (228 Ω) was the lowest among the films which signified the highest electric conductivity. A gentler Warburg line in the rGO/TiO₂/MnO₂ electrode suggested a larger Li⁺ diffusion barrier (thus, slower Li-ion diffusion kinetics) compared to the former materials. Moreover, all semicircles were incomplete which implied poor electronic transport. Additionally, Figure S7 shows the Nyquist plots of pristine TiO₂ and MnO₂. The TiO₂ electrode (Figure S7a) behaved similarly to the rGO-based anodes. An incomplete semicircle indicated mediocre electron transfer and a steep Warburg line indicated efficient lithium-ion diffusion through the active material. Due to an increased amount of carbon black, the MnO₂ (Figure S7b) electrode exhibited lower R_{ct} (75.23 Ω) in contrast to 156.9 Ω of TiO₂. Moreover, the semicircle was completed, which implies much better electron transfer due to an excess of conductive carbon black.

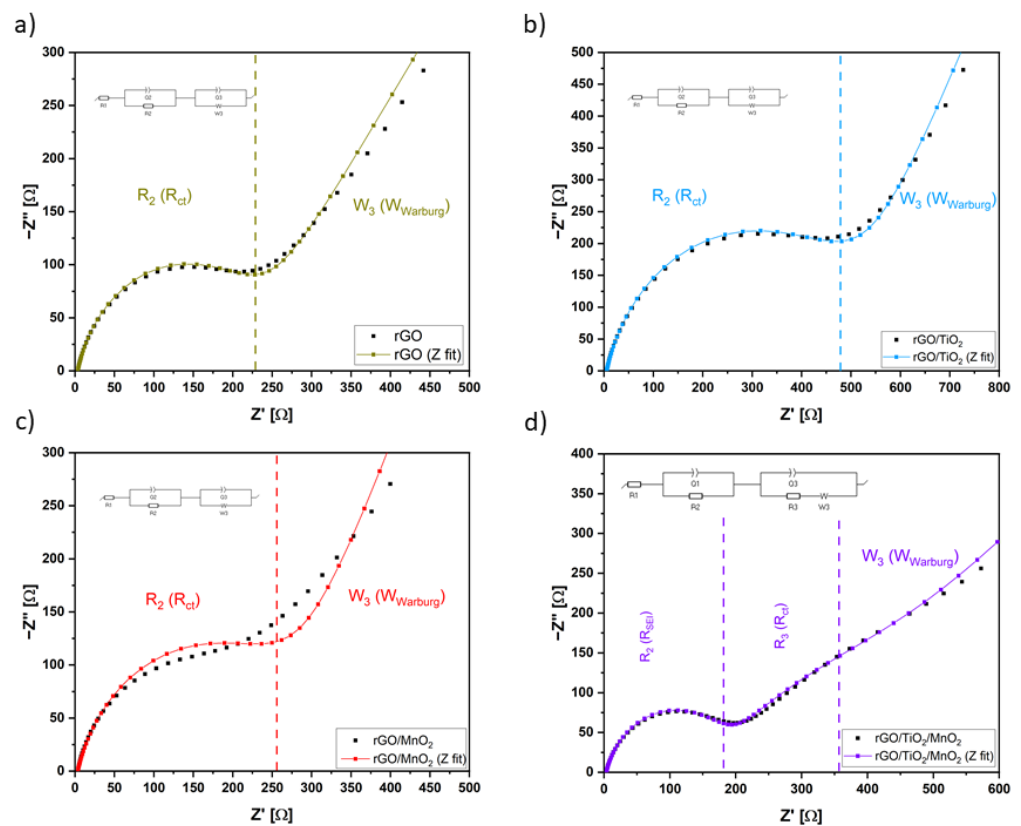


Figure 10. Nyquist plots of (a) rGO, (b) rGO/TiO₂, (c) rGO/MnO₂ and (d) rGO/TiO₂/MnO₂ after discharge/charge cycles and the equivalent circuit diagrams of the cells.

Table 2. Fitted results of the equivalent circuit in Figure 10.

Film	R_S [Ω]	R_{SEI} [Ω]	R_{ct} [Ω]
rGO	3.24	-	228
rGO/TiO ₂	5.07	-	481.7
rGO/MnO ₂	3.19	-	257.5
rGO/TiO ₂ /MnO ₂	3.28	181.1	351.5

4. Conclusions

In summary, the free-standing and non-active-material-free rGO, rGO/TiO₂, rGO/MnO₂ and rGO/TiO₂/MnO₂ films were assembled using vacuum-assisted filtration. rGO/TiO₂/MnO₂ attained a stable reversible capacity (353 mAh/g after 50 cycles), great cyclic stability and an outstanding rate performance. The SEI layer formed during discharging/charging was thin enough to allow smooth lithium diffusion, increasing the kinetics of the electrochemical reactions. Furthermore, reduced graphene oxide acted as the conductive agent, as well as the active material, making the electrode free of the binding agent. Additionally, the free-standing nature of the films did not require the current collector and their preparation did not utilize any harmful substances. As a result, no excess mass nor volume were reported. It is important to note that the films displayed flexibility, making them promising candidates as electrodes in rechargeable batteries for flexible electronics.

Supplementary Materials: The following are available online at <https://www.mdpi.com/article/10.3390/en14238168/s1>, Figure S1: TEM images of (a,b) MnO₂ and (c,d) TiO₂, Figure S2: XRD diffractograms of TiO₂ and MnO₂, Figure S3. Raman spectra of TiO₂ and MnO₂, Figure S4. Cyclic voltammetry of pristine (a) TiO₂ and (b) MnO₂, Figure S5. Discharge–charge profiles of (a) TiO₂ and (b) MnO₂ at a current density of 50 mA/g, Figure S6. Rate performance of (a) TiO₂ and (b) MnO₂ at different current densities, Figure S7. Nyquist plots of (a) TiO₂ and (b) MnO₂ after discharge/charge cycles and the equivalent circuit diagrams of the cells, Table S1. Fitted results of the equivalent circuit in Figure S7.

Author Contributions: Conceptualization, B.Z., X.C. and E.M.; Investigation, T.K. and D.B. (Damian Bęben); Methodology, T.K., D.B. (Daria Baranowska) and D.B. (Damian Bęben); Supervision, B.Z., X.C. and E.M.; Visualization, T.K.; Writing—original draft, T.K.; Writing—review & editing, D.B. (Daria Baranowska), B.Z., X.C. and E.M. All authors have read and agreed to the published version of the manuscript.

Funding: Not applicable.

Data Availability Statement: Not applicable.

Conflicts of Interest: The authors declare no conflict of interest.

References

- Liu, W.; Song, M.-S.; Kong, B.; Cui, Y. Flexible and Stretchable Energy Storage: Recent Advances and Future Perspectives. *Adv. Mater.* **2017**, *29*, 1603436. [[CrossRef](#)]
- Lin, L.; Ning, H.; Song, S.; Xu, C.; Hu, N. Flexible Electrochemical Energy Storage: The Role of Composite Materials. *Compos. Sci. Technol.* **2020**, *192*, 108102. [[CrossRef](#)]
- Mo, R.; Rooney, D.; Sun, K. Hierarchical Graphene-Scaffolded Mesoporous Germanium Dioxide Nanostructure for High-Performance Flexible Lithium-Ion Batteries. *Energy Storage Mater.* **2020**, *29*, 198–206. [[CrossRef](#)]
- Nitta, N.; Wu, F.; Lee, J.T.; Yushin, G. Li-Ion Battery Materials: Present and Future. *Mater. Today* **2015**, *18*, 252–264. [[CrossRef](#)]
- Singh, V.; Joung, D.; Zhai, L.; Das, S.; Khondaker, S.I.; Seal, S. Graphene Based Materials: Past, Present and Future. *Prog. Mater. Sci.* **2011**, *56*, 1178–1271. [[CrossRef](#)]
- Peng, Z.; Zhang, H.; Ali, I.; Li, J.; Ding, Y.; Deng, L.; Han, T.; Zhu, H.; Zeng, X.; Cheng, D.; et al. A Rod-on-Tube CoMoO₄@hydrogel Composite as Lithium-Ion Battery Anode with High Capacity and Stable Rate-Performance. *J. Alloys Compd.* **2021**, *858*, 157648. [[CrossRef](#)]
- Tariq, Z.; Rehman, S.U.; Zhang, J.; Butt, F.K.; Zhang, X.; Cheng, B.; Zahra, S.; Li, C. Hierarchical Mesoporous Nanoflowers of Zn₂VO₄ for High Capacity Anode in Lithium Ion Batteries. *Mater. Sci. Semicond. Process.* **2021**, *123*, 105549. [[CrossRef](#)]

8. di Lecce, D.; Andreotti, P.; Boni, M.; Gasparro, G.; Rizzati, G.; Hwang, J.-Y.; Sun, Y.-K.; Hassoun, J. Multiwalled Carbon Nanotubes Anode in Lithium-Ion Battery with LiCoO_2 , $\text{Li}[\text{Ni}_{1/3}\text{Co}_{1/3}\text{Mn}_{1/3}]\text{O}_2$, and $\text{LiFe}_{1/4}\text{Mn}_{1/2}\text{Co}_{1/4}\text{PO}_4$ Cathodes. *ACS Sustain. Chem. Eng.* **2018**, *6*, 3225–3232. [[CrossRef](#)]
9. Srinivaas, M.; Wu, C.-Y.; Duh, J.-G.; Hu, Y.-C.; Wu, J.M. Multi-Walled Carbon-Nanotube-Decorated Tungsten Ditelluride Nanostars as Anode Material for Lithium-Ion Batteries. *Nanotechnology* **2020**, *31*, 035406. [[CrossRef](#)]
10. Khomenko, V.G.; Barsukov, V.Z.; Doninger, J.E.; Barsukov, I.V. Lithium-Ion Batteries Based on Carbon–Silicon–Graphite Composite Anodes. *J. Power Sources* **2007**, *165*, 598–608. [[CrossRef](#)]
11. Yang, M.; Ko, S.; Im, J.S.; Choi, B.G. Free-Standing Molybdenum Disulfide/Graphene Composite Paper as a Binder- and Carbon-Free Anode for Lithium-Ion Batteries. *J. Power Sources* **2015**, *288*, 76–81. [[CrossRef](#)]
12. Stoller, M.D.; Park, S.; Zhu, Y.; An, J.; Ruoff, R.S. Graphene-Based Ultracapacitors. *Nano Lett.* **2008**, *8*, 3498–3502. [[CrossRef](#)]
13. Balandin, A.A.; Ghosh, S.; Bao, W.; Calizo, I.; Teweldebrhan, D.; Miao, F.; Lau, C.N. Superior Thermal Conductivity of Single-Layer Graphene. *Nano Lett.* **2008**, *8*, 902–907. [[CrossRef](#)] [[PubMed](#)]
14. Novoselov, K.S. Electric Field Effect in Atomically Thin Carbon Films. *Science* **2004**, *306*, 666–669. [[CrossRef](#)]
15. He, Q.; Sudibya, H.G.; Yin, Z.; Wu, S.; Li, H.; Boey, F.; Huang, W.; Chen, P.; Zhang, H. Centimeter-Long and Large-Scale Micropatterns of Reduced Graphene Oxide Films: Fabrication and Sensing Applications. *ACS Nano* **2010**, *4*, 3201–3208. [[CrossRef](#)]
16. Wu, S.; Yin, Z.; He, Q.; Huang, X.; Zhou, X.; Zhang, H. Electrochemical Deposition of Semiconductor Oxides on Reduced Graphene Oxide-Based Flexible, Transparent, and Conductive Electrodes. *J. Phys. Chem. C* **2010**, *114*, 11816–11821. [[CrossRef](#)]
17. Rowden, B.; Garcia-Araez, N. Estimating Lithium-Ion Battery Behavior from Half-Cell Data. *Energy Rep.* **2021**, *7*, 97–103. [[CrossRef](#)]
18. Joshi, B.; Samuel, E.; Kim, M.-W.; Kim, K.; Kim, T.-G.; Swihart, M.T.; Yoon, W.Y.; Yoon, S.S. Electrospayed Graphene Films Decorated with Bimetallic (Zinc-Iron) Oxide for Lithium-Ion Battery Anodes. *J. Alloys Compd.* **2019**, *782*, 699–708. [[CrossRef](#)]
19. Dong, Y.; Chen, S.; Liu, J.; Lei, J.; Liu, F.; Yang, W.; Wang, J. Polygonal WS_2 -Decorated-Graphene Multilayer Films with Microcavities Prepared from a Cheap Precursor as Anode Materials for Lithium-Ion Batteries. *Mater. Lett.* **2019**, *254*, 73–76. [[CrossRef](#)]
20. Fang, D.; Ji, Y.; Sun, B.; Bao, R.; Yi, J.; Luo, Z. Cobalt Oxide Nanoparticles Anchored on Discharged-Graphene Film for Lithium-Ion Battery. *Solid State Ion.* **2019**, *340*, 115006. [[CrossRef](#)]
21. Dong, L.; Li, M.; Dong, L.; Zhao, M.; Feng, J.; Han, Y.; Deng, J.; Li, X.; Li, D.; Sun, X. Hydrothermal Synthesis of Mixed Crystal Phases TiO_2 -Reduced Graphene Oxide Nanocomposites with Small Particle Size for Lithium Ion Batteries. *Int. J. Hydrogen Energy* **2014**, *39*, 16116–16122. [[CrossRef](#)]
22. Tang, Y.; Wang, S.; Tan, X.; Hou, G.; Zheng, G. TiO_2 /Graphene Nanocomposites as Anode Materials for High Rate Lithium-Ion Batteries. *J. Cent. South Univ.* **2014**, *21*, 1714–1718. [[CrossRef](#)]
23. Xu, T.; Meng, Q.; Fan, Q.; Yang, M.; Zhi, W.; Cao, B. Electrophoretic Deposition of Binder-Free MnO_2 /Graphene Films for Lithium-Ion Batteries. *Chin. J. Chem.* **2017**, *35*, 1575–1585. [[CrossRef](#)]
24. Cao, H.; Suib, S.L. Highly Efficient Heterogeneous Photooxidation of 2-Propanol to Acetone with Amorphous Manganese Oxide Catalysts. *J. Am. Chem. Soc.* **1994**, *116*, 5334–5342. [[CrossRef](#)]
25. Wei, X.; Zhu, G.; Fang, J.; Chen, J. Synthesis, Characterization, and Photocatalysis of Well-Dispersible Phase-Pure Anatase TiO_2 Nanoparticles. *Int. J. Photoenergy* **2013**, *2013*, 1–6. [[CrossRef](#)]
26. Radoń, A.; Włodarczyk, P.; Łukowiec, D. Structure, Temperature and Frequency Dependent Electrical Conductivity of Oxidized and Reduced Electrochemically Exfoliated Graphite. *Phys. E Low-Dimens. Syst. Nanostruct.* **2018**, *99*, 82–90. [[CrossRef](#)]
27. Challagulla, S.; Tarafder, K.; Ganesan, R.; Roy, S. Structure Sensitive Photocatalytic Reduction of Nitroarenes over TiO_2 . *Sci. Rep.* **2017**, *7*, 8783. [[CrossRef](#)] [[PubMed](#)]
28. Zhang, L. Fabrication of $\beta\text{-MnO}_2$ /RGO Composite and Its Electrochemical Properties. *Int. J. Electrochem. Sci.* **2016**, *11*, 10815–10826. [[CrossRef](#)]
29. Kernazhitsky, L.; Shymanovska, V.; Gavrilko, T.; Puchkovska, G.; Naumov, V.; Khalyavka, T.; Kshnyakin, V.; Chernyak, V.; Baran, J. Optical and Photocatalytic Properties of Titanium–Manganese Mixed Oxides. *Mater. Sci. Eng. B* **2010**, *175*, 48–55. [[CrossRef](#)]
30. Cheng, S.; Yang, L.; Chen, D.; Ji, X.; Jiang, Z.; Ding, D.; Liu, M. Phase Evolution of an Alpha MnO_2 -Based Electrode for Pseudo-Capacitors Probed by in Operando Raman Spectroscopy. *Nano Energy* **2014**, *9*, 161–167. [[CrossRef](#)]
31. van de Krol, R.; Goossens, A.; Schoonman, J. Spatial Extent of Lithium Intercalation in Anatase TiO_2 . *J. Phys. Chem. B* **1999**, *103*, 7151–7159. [[CrossRef](#)]
32. Han, Q.; Zhang, W.; Han, Z.; Wang, F.; Geng, D.; Li, X.; Li, Y.; Zhang, X. Preparation of PAN-Based Carbon Fiber@ MnO_2 Composite as an Anode Material for Structural Lithium-Ion Batteries. *J. Mater. Sci.* **2019**, *54*, 11972–11982. [[CrossRef](#)]